

## Article

# Characterization of Nanosized Carbide Precipitates in Multiple Microalloyed Press Hardening Steels

Hardy Mohrbacher <sup>1,2,\*</sup> , Linda Bacchi <sup>3</sup>, Gloria Ischia <sup>4</sup> , Stefano Gialanella <sup>4</sup>, Michele Tedesco <sup>5</sup>, Fabio D'Aiuto <sup>6</sup> and Renzo Valentini <sup>7</sup> 

<sup>1</sup> NiobelCon BV, 2970 Schilde, Belgium

<sup>2</sup> Department of Materials Engineering (MTM), KU Leuven, 3001 Leuven, Belgium

<sup>3</sup> R&D Department, Letomec S.r.l., 56126 Pisa, Italy

<sup>4</sup> Department of Industrial Engineering, University of Trento, 38123 Trento, Italy

<sup>5</sup> Metals Department, Centro Ricerche Fiat S.C.p.A, 10135 Turin, Italy

<sup>6</sup> CBMM Asia Pte Ltd., Singapore 049315, Singapore

<sup>7</sup> Department of Civil and Industrial Engineering, Pisa University, 56122 Pisa, Italy

\* Correspondence: hm@niobelcon.net

**Abstract:** Press hardening steel standardly relies on titanium microalloying for protecting boron from being tied up by residual nitrogen. This practice safeguards the hardenability effect of boron during die quenching. More recently, additional microalloying elements were added to press hardening steel to further improve properties and service performance. Niobium was found to induce microstructural refinement, leading to better toughness, bendability, and hydrogen embrittlement resistance. In that respect, niobium also extends the operating window of the press hardening process. Vanadium microalloying has been proposed to provide hydrogen trapping by its carbide precipitates. A recently developed press hardening steel employs all three microalloying elements in an attempt to further enhance performance. The current study analyses the microstructure of such multiple microalloyed press hardening steel, and compares it to the standard grade. Particularly, the effect of various heat treatments is investigated, indicating that the multiple microalloyed steel is more resistant against grain coarsening. TEM analysis is used to identify the various particle species formed in the steels, to track their formation, and to determine their size distributions. Nanosized microalloy carbide particles typically comprise a mixed composition involving niobium, titanium, and vanadium. Furthermore, these precipitates are incoherent to the matrix. Regarding tensile properties, it is found that the multiple microalloyed press hardening steel is superior to the standard grade.

**Keywords:** press hardening steel; grain coarsening resistance; particle dispersion; microalloy solubility; microalloy diffusion; segregation; particle strengthening; transitional iron carbides



**Citation:** Mohrbacher, H.; Bacchi, L.; Ischia, G.; Gialanella, S.; Tedesco, M.; D'Aiuto, F.; Valentini, R.

Characterization of Nanosized Carbide Precipitates in Multiple Microalloyed Press Hardening Steels. *Metals* **2023**, *13*, 894. <https://doi.org/10.3390/met13050894>

Academic Editor: Chengbin Shi

Received: 24 March 2023

Revised: 25 April 2023

Accepted: 3 May 2023

Published: 5 May 2023



**Copyright:** © 2023 by the authors. Licensee MDPI, Basel, Switzerland. This article is an open access article distributed under the terms and conditions of the Creative Commons Attribution (CC BY) license (<https://creativecommons.org/licenses/by/4.0/>).

## 1. Introduction

Press hardening steel (PHS) attains its ultrahigh strength by heating up the original ferritic–pearlitic microstructure into the austenite range, before stamping and in situ quenching to martensite after die closure. An alloy concept containing manganese, boron, and titanium is standardly used to provide sufficient hardenability in this process. Boron is microalloyed to an ideal amount of 15–20 ppm for preventing nucleation of ferrite or bainite at austenite grain boundaries. Titanium microalloying protects boron from forming a boron nitride compound, which would otherwise result in the loss of its hardenability effect. The titanium microalloy addition must be coordinated with the residual nitrogen content in the steel, which ranges between 30 and 120 ppm depending on the steelmaking process. Titanium should be added to an ideal amount meeting the stoichiometric mass ratio of Ti:N = 3.4 to tie up all residual nitrogen. Overstoichiometric titanium addition, however, can result in the formation of micrometer-sized TiN particles during steel solidification. Such coarse particles are harmful to toughness, crash, and forming properties [1,2]. This

situation is aggravated when the residual nitrogen content is simultaneously on the high side, as is typically the case for electric arc furnace (EAF) steelmaking.

Nanosized precipitates of microalloy carbides play an important role for optimizing application-relevant properties of martensitic steels [3]. Such particles have been shown to restrict austenite grain size and to provide a more homogeneous grain size distribution during heat treatment, resulting in better toughness and increased critical bending angle (VDA238-100) [4–6]. Furthermore, nanoprecipitates have been indicated as acting as potential trapping sites for hydrogen, thus improving delayed cracking resistance [7–11]. In either respect, it is desirable to have a high number of particles with uniform spatial distribution and sufficient temperature stability over the entire duration of the heat treatment. Niobium and titanium are strong carbide formers, with low solubility in austenite and ferrite. This provides good particle stability at typical heat treatment temperatures. However, it also limits the total amount that can be brought into solution during slab soaking, considering the carbon content used in PHS. Vanadium, on the contrary, can be added to a comparably large amount due to its good solubility in austenite. Consequently, the stability of vanadium carbide precipitates, especially in austenite, at the temperature of PHS heat treatment is limited.

Principally, titanium carbide particles can only form when added overstoichiometric to nitrogen. This may result in the unwanted formation of coarse TiN particles, as outlined before and, thus, is a constraining criterion. Niobium, on the other hand, primarily precipitates nanosized carbide particles. To some extent, it forms epitaxially grown NbC shells on existing TiN particles [12]. That share of niobium is metallurgically ineffective. Due to the beneficial effects of NbC nanoparticles, niobium microalloying is already being used in commercial PHS grades, particularly in grades with 1800–2000 MPa strength [11,13–16]. Recently, some PHS alloy developments proposed incorporating vanadium microalloying, either as dual Ti–V steel or as triple microalloyed Ti–Nb–V steel. For dual Ti–V steels, rather high vanadium additions, up to 0.2 mass percent, were reported [8,17], whereas in triple Ti–Nb–V, all three microalloying elements were typically added in the same range of 0.02–0.04% [7,18]. Higher vanadium additions are common in quenched and tempered martensitic steels. Prominent vanadium carbide precipitation occurs when tempering in the temperature range of 500–650 °C, providing pronounced secondary hardening. However, during manufacturing of PHS components, the quenched steel is only exposed to low-temperature tempering, during paint baking, at around 170 °C. This condition does not enable microalloy precipitation. For triple microalloyed PHS, it was argued that a higher particle density would provide additional grain refinement and enhance hydrogen trapping [7,18]. However, the results reported so far indicate that a triple microalloyed TiNbV PHS has negligible advantage over dual microalloyed TiNb PHS. Thus, the question remains whether such triple microalloyed PHS effectively contains more numerous and/or stable carbide precipitates.

The current study provides a detailed microstructural analysis of commercially available triple microalloyed PHS in comparison to an established single microalloyed reference. Thereby, overheating conditions, in addition to standard heat treatment practices, are applied. Transmission electron microscopy is employed to characterize the particle size distribution, as well as the particle composition, under different austenitizing conditions. The prior austenite grain size and tensile characteristics of the quenched steels are correlated with the precipitation status. The results are interpreted using established solubility equations. A comparison to dual microalloyed TiNb PHS grades, investigated earlier, allows for judging the potential benefit of the more costly triple microalloy concept.

## 2. Materials and Methods

Two 22MnB5 steels with different alloy concepts (Table 1) originating from industrial production were evaluated in this study. Both steels were AlSi coated (AS40) after cold rolling to 1.2 mm final sheet gage. The processing history of these steels is schematically shown in Figure 1. Slab soaking was performed at 1230 °C to bring the microalloying

elements into solid solution. Hot rolling was finished at 890 °C and followed by coiling at 650 °C. Cold rolling with a reduction of approximately 60% was followed by continuous annealing at a peak metal temperature of 790 °C, and subsequent AlSi hot dip coating at 680 °C. Individual sheets were cut from the produced coils and heated up in a laboratory furnace, and held at various austenitizing temperatures and dwell times. The standard treatment in this study is defined as austenitizing the steel at a temperature of 915 °C for 8 min. In addition, overheating conditions were simulated by either applying an extended holding time of 25 min, an elevated austenitizing temperature of 970 °C, or both. Subsequently, the sheets were quenched in hot water (80 °C). Part of the samples were subjected to a paint baking heat cycle at a temperature of 170 °C for 20 min. Characterization of the mechanical properties was conducted in the cold rolled (i.e., before heat treatment) and as-quenched condition using standard tensile testing with a quasi-static strain rate of 0.001 s<sup>-1</sup> and a sample gage length of 80 mm.

**Table 1.** Chemical composition of 22MnB5 press hardening steels (n.a.: not alloyed).

	C	Si	Mn	Cr	N	Ti	Nb	V	B	P	S
Standard PHS	0.24	0.25	1.31	0.18	0.003	0.03	n.a.	n.a.	0.002	0.01	0.001
NbV PHS	0.20	0.28	1.21	0.17	0.003	0.03	0.04	0.04	0.002	0.01	0.001

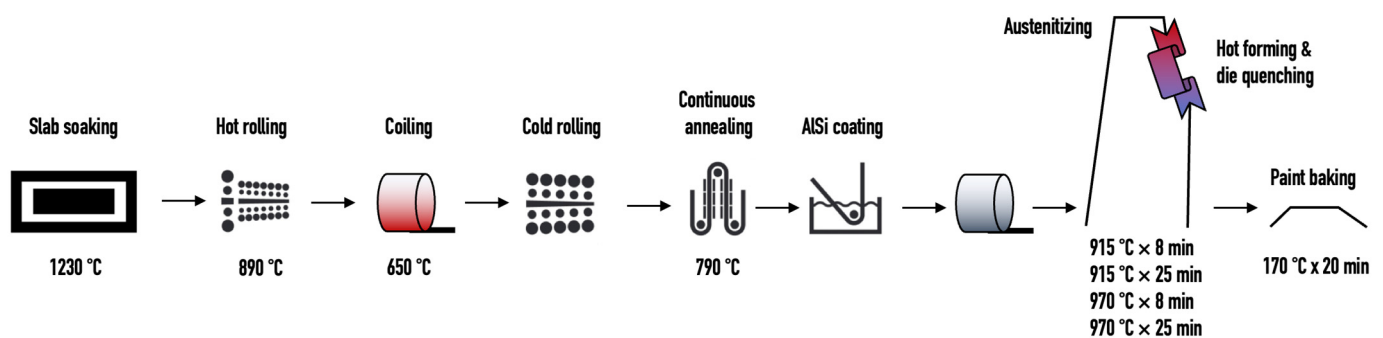


**Figure 1.** Processing history of the investigated press hardening steels indicating relevant treatment temperatures with regard to microalloy precipitation.

For metallographic analysis of the various processing conditions, samples were polished and etched with nital for observation by light optical microscopy. This procedure allowed visualizing the presence of coarse TiN precipitates. To determine the PAGS, samples were etched with a saturated aqueous picric acid solution with the addition of a wetting agent, sodium alkylsulfonate (Teepol, London, UK). The PAGS was measured on light optical micrographs using a linear intercept procedure [19]. The average PAGS values from 10 selected view fields are represented as a minimum–maximum range. More detailed microstructural analysis employed transmission electron microscopy. The samples were observed with a scanning transmission electron microscope (S/TEM), ThermoFisher TALOS F200S (Thermo Fisher Scientific Inc., Waltham, MA, USA), at a maximum electron voltage of 200 kV. The instrument is equipped with an energy dispersive X-ray spectrometer (EDXS) system provided with two windowless silicon drift detectors (SDDs) for a total active area of 60 mm<sup>2</sup>, which allow high-resolution elemental analyses and maps. TEM samples were prepared starting from 1 mm thick material slices, mechanically polished on both sides down to a thickness of about 100 µm, and a surface roughness of 1 µm. Three-millimeter discs were punched from the thin foil, dimple-ground in the central area down to 20 µm thickness, and electrochemically polished down to electron transparency in a TenuPol-5 Struers apparatus. The electrochemical thinning was carried out using a solution of 10% perchloric acid in 2-butoxy-ethanol at a temperature of 5 °C, an applied voltage of 40 V, and a current of 4 mA.

### 3. Results

The following section reports the measured characteristics of both steel alloys in direct comparison, firstly for the as-delivered condition, and subsequently after heat treatment.

#### 3.1. Mechanical and Microstructural Characteristics before Heat Treatment

Light optical metallography of the cold rolled annealed steels reveals a finer microstructure in the triple microalloyed PHS as compared to the standard PHS (Figure 2a,b). Ferrite and pearlite phases are aggregated in a banded structure parallel to the direction of cold rolling. The average ferritic grain size dimensions are between 5.5 and 7.2  $\mu\text{m}$  (ASTM G 11.5) in the standard PHS, and between 5.0 and 5.5  $\mu\text{m}$  (ASTM G 12) in the NbV microalloyed PHS. The pearlite island size is also refined in the NbV microalloyed variant. Individual TiN particles of several micrometers in size can be seen in both steel alloys. It appears that these are mostly associated with pearlite bands, suggesting that titanium segregation during solidification is the origin of primary particle formation in the liquid phase. TEM micrography could identify ferrite and pearlite grains in the lower micrometer size range, as well as cementite particles in the size range of around 100 nm. Such cementite particles are enriched with manganese and chromium.

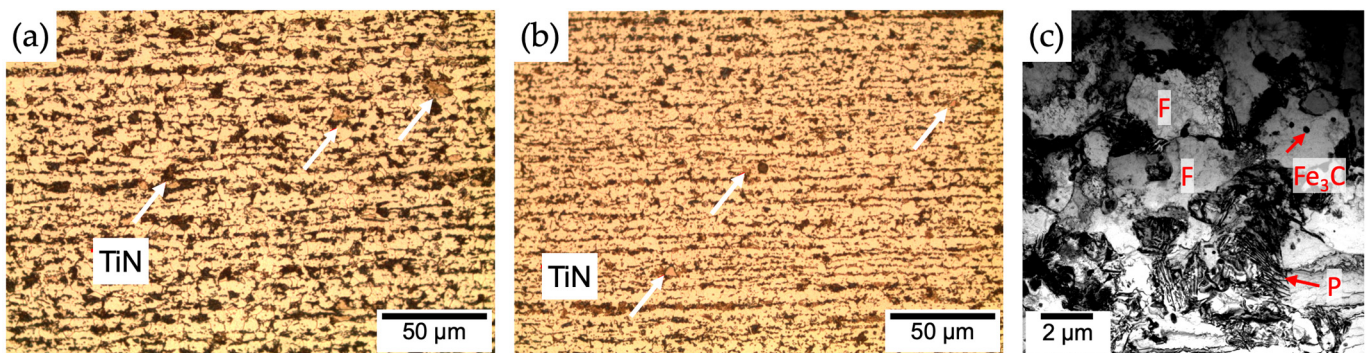


**Figure 2.** Optical microstructure of cold rolled annealed sheets of (a) standard 22MnB5 and (b) NbV microalloyed PHS; TiN particles indicated by arrows. (c) TEM micrograph identifying ferrite (F), pearlite (P), and cementite ( $\text{Fe}_3\text{C}$ ) constituents in the NbV microalloyed PHS.

A more detailed TEM analysis of the standard PHS revealed a particle population with square-shaped morphology, and dimensions ranging between 50 and 200 nm. These appear to be randomly distributed in the microstructure, composed of titanium in the form of  $\text{Ti}(\text{C},\text{N})$  or  $\text{Ti}_4\text{C}_2\text{S}_2$ . Titanium is known to form  $\text{Ti}_4\text{C}_2\text{S}_2$  in association with MnS or CuS particles, which act as heterogeneous nucleation sites. Some TiN particles comprised an epitaxially grown NbC layer, indicating that the full amount of niobium was not available for nanocarbide formation.

In the NbV microalloyed steel, spheroidal precipitates are observed inside ferritic grains (Figure 3). These particles have diameters between 8 and 35 nanometers. EDX analysis indicates a mixed particle composition involving Ti, V, Nb, and sometimes traces of Mo. Since molybdenum was not intentionally alloyed to this steel, it must have been retained in residual amounts from scrap additions. The composition of individual particles is given as the microalloy atom fraction normalized to the carbon fraction in Table 2. Accordingly, particles A–C have carbon excess, whereas D is carbon substoichiometric, and E can be considered stoichiometric in terms of an MC-type compound. Vanadium has the highest atom share available for carbide precipitation in ferrite, being approximately twice that of titanium and niobium after correcting their losses into early forming nitride and carbo-sulfide particles. However, only particle D reflects a high atom ratio of vanadium. In the other observed particles, vanadium is under-represented. This aspect will be discussed in detail later (see Section 4).

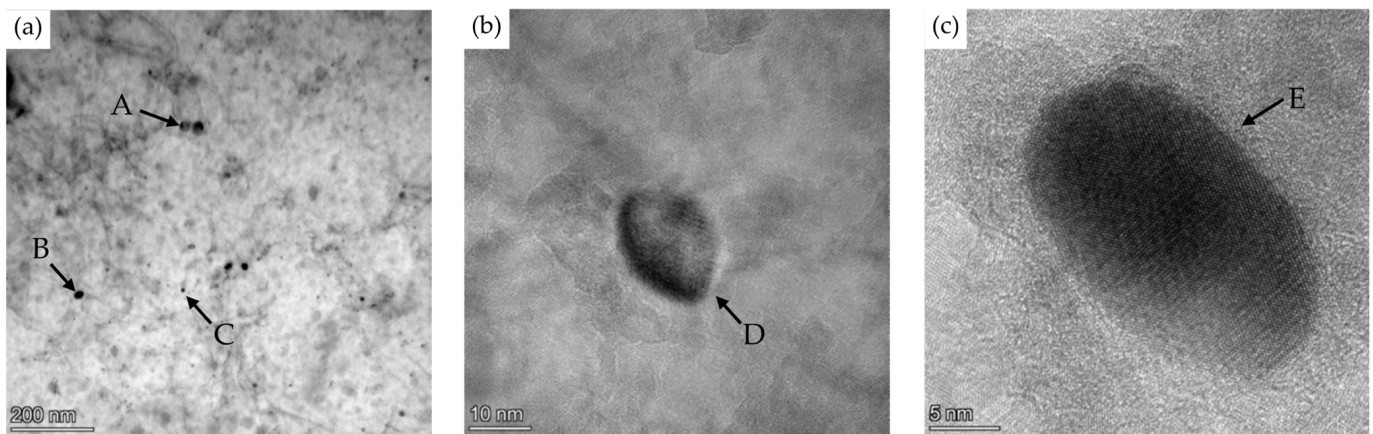


**Figure 3.** (a) TEM analysis of nanocarbided in the ferrite matrix of NbV microalloyed PHS (b,c).

**Table 2.** Atom fraction of microalloying elements in particles A–E identified in Figure 3.

Particle	Ti	Nb	V	Mo	Sum
A	0.29	0.17	0.26	0.12	0.84
B	0.35	0.23	0.15	0.09	0.82
C	0.16	0.13	0.12	0.06	0.47
D	0.40	0.31	0.77	0.04	1.52
E	0.42	0.39	0.24	0.00	1.05

The mechanical properties of these steels, obtained by tensile testing, are summarized in Table 3. Both steels present continuous yielding and similar work hardening behavior. The NbV microalloyed PHS has marginally higher strength and obviously better total elongation. The latter can be related to a smaller pearlite volume fraction due to the lower carbon content, as well as to a more homogeneous distribution of pearlite (Figure 2b). In terms of strength, the reduced pearlite content is compensated by the finer ferrite grain size and the population of nanosized carbides. Considering the property differences in the longitudinal and transverse directions, the NbV PHS has a very high isotropy.

**Table 3.** Mechanical properties of cold rolled annealed steels obtained by tensile testing (average values of three individual tests).

Test Direction	Standard PHS		NbV PHS	
	Longitudinal	Transverse	Longitudinal	Transverse
Yield strength $R_{p0.2}$ (MPa)	462	445	454	452
Tensile strength $R_m$ (MPa)	665	652	668	679
Total elongation $A_{80}$ (%)	19	16	20	22

### 3.2. Mechanical and Microstructural Characteristics after Reference Heat Treatment

After austenitizing the steels at 915 °C for 8 min, followed by simulated die quenching, transformation into a fully martensitic microstructure is achieved. This reflects in the tensile characteristics and the microstructure (Figure 4). The properties shown in Table 4 fulfil the requirements of a 1500 MPa PHS (specified tensile strength range 1300–1650 MPa) for both alloys, despite the carbon difference of 0.04% (Table 1).

According to the relationships established for martensitic steels, this carbon variation of 0.04% should result in an approximately 140 MPa difference in tensile strengths [3]. It is reasonable to assume that microalloy nanoparticles and microstructural refinement must have compensated the carbon-related strength loss in the NbV PHS. The total elongation of 4–6% is typical for fully quenched martensite of this strength level, but appears to be somewhat higher in the NbV PHS as compared to the standard PHS. The prior austenite grain size (PAGS) in the NbV PHS is approximately 5  $\mu\text{m}$  smaller as compared to the standard

PHS. This PAGES refinement can provide a strength increase of around 30 MPa, estimated from the Hall–Petch relationship. The precipitation-related strength increase in dual (NbTi) microalloyed PHS has been estimated previously, according to the Ashby–Orowan approach, being in the order of 100 MPa [20]. Thus, both mechanisms together can indeed compensate for the strength difference related to the 0.04% difference in the carbon content.

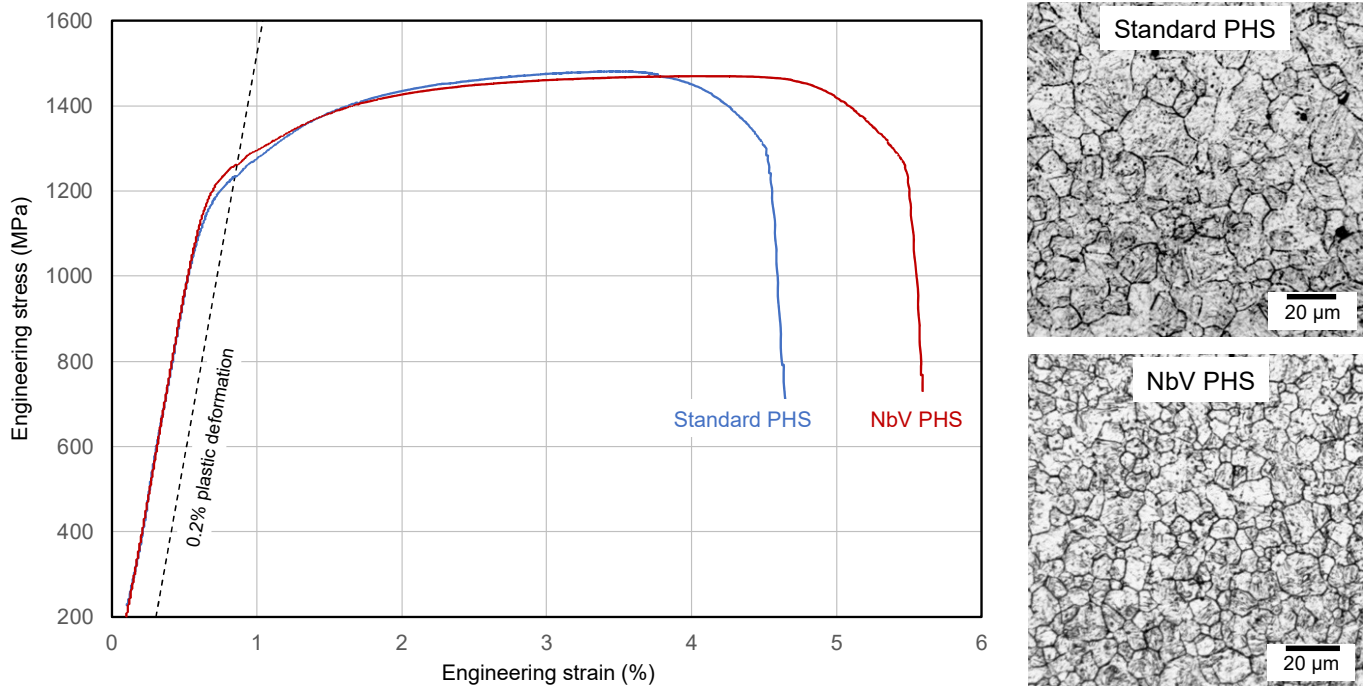


**Figure 4.** Tensile curves and prior austenite grain structure of the steel alloys after reference heat treatment (915 °C for 8 min) and simulated die quenching.

**Table 4.** Mechanical properties (average values of three individual tests) and prior austenite grain size (PAGS) of the steel alloys after reference heat treatment (915 °C for 8 min) and simulated die quenching.

	Standard PHS	NbV PHS
Yield strength $R_{p0.2}$ (MPa)	1231	1262
Tensile strength $R_m$ (MPa)	1470	1462
Total elongation $A_{80}$ (%)	4.6	5.4
PAGS ( $\mu\text{m}$ )	15–20 (ASTM G 8.5)	10–15 (ASTM G 9.5)

The TEM particle analysis in the standard PHS revealed a principally similar precipitate population, as already reported for the cold rolled annealed condition. Accordingly, the heat treatment cycle had little influence in this respect. TiC nanoprecipitates were not detected. In the NbV PHS, however, a bimodal particle population is present after the heat treatment (Figure 5). Larger sized precipitates have dimensions varying between 100 and 200 nanometers (Figure 6a). The EDX spectra indicate that these precipitates have two different compositions. Some of them are mixed Ti–Nb-based carbides or carbonitrides, typically having a cube-shaped morphology. Others, possibly being carbo–sulfides, show an enrichment of Cr, Mn, V, and a small amount of copper. Based on these observations, it can be inferred that vanadium inside such coarser particles is absent and limited to the segregation of solute vanadium at the particle–matrix interface. The distribution diagram reveals a prominent fraction of fine-sized carbide precipitates (Figure 6b), being mainly composed of Ti, Nb, and V (Figure 6c). Semiquantitative analysis of the EDX spectra allowed to determine the composition ratios of such particles. Spectra were taken at ten

different positions (Figure 6d), and the atom fractions of microalloying elements were determined using the titanium peak as a reference (Table 5). The average composition of the analysed particles consists of nearly equal numbers of niobium and titanium atoms, whereas vanadium atoms are represented by a smaller share.

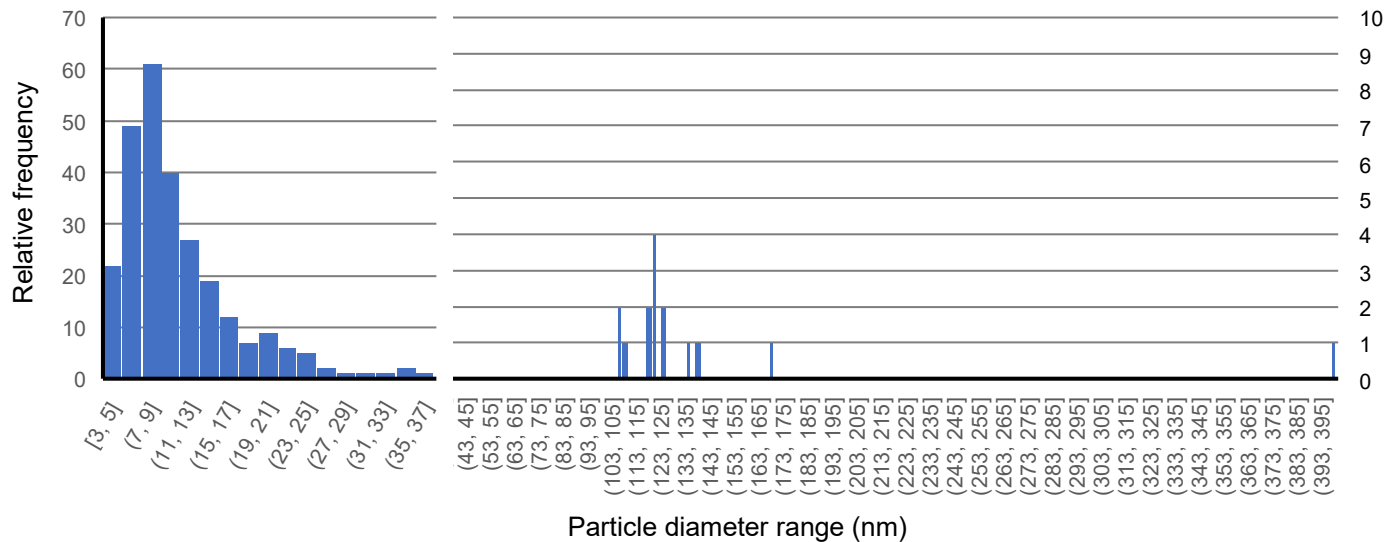


Figure 5. Particle size distribution in the NbV PHS after the reference heat treatment.

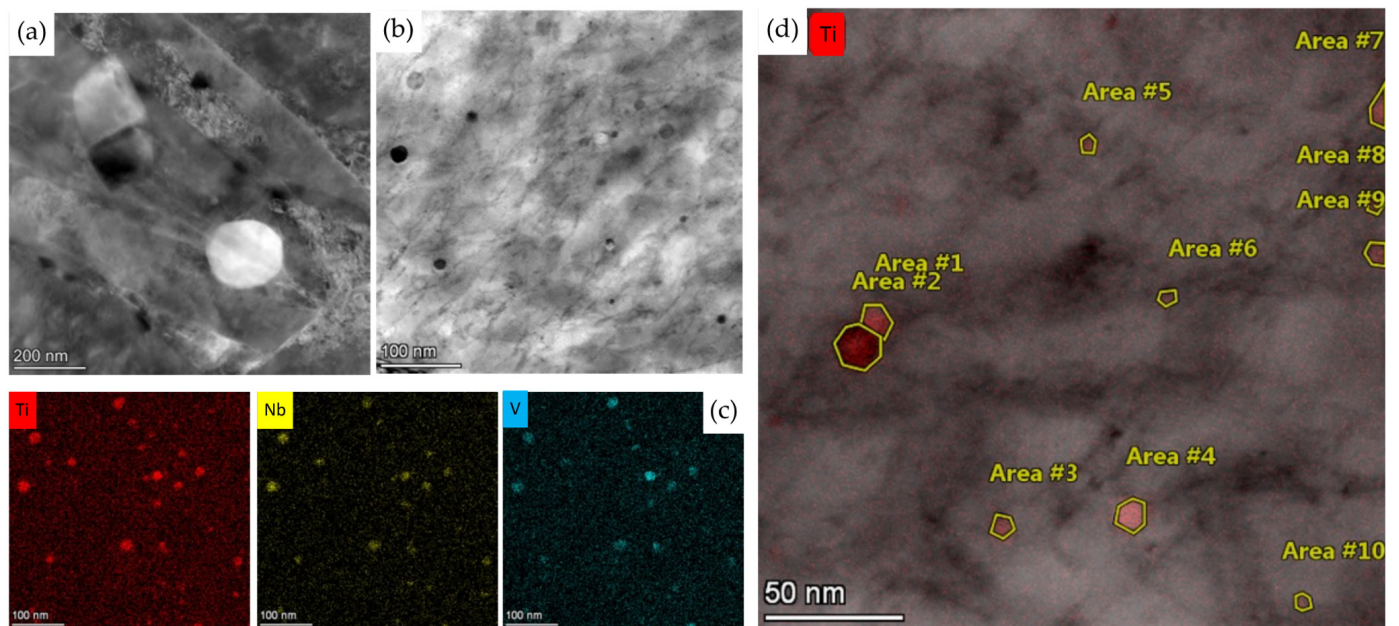


Figure 6. TEM micrographs of (a) coarser particles and (b) ultrafine particles in the NbV PHS after the reference heat treatment. (c) EDX mapping of the particles shown in (b). (d) Positions for semiquantitative analysis of particle composition from EDX spectra (see Table 5).

Table 5. Atomic ratio of Nb and V in selected particles (areas in Figure 6d) normalized to Ti.

Area	#1	#2	#3	#4	#5	#6	#7	#8	#9	#10	Ave.
Ti	1	1	1	1	1	1	1	1	1	1	1
V	0.39	0.41	0.73	0.39	0.50	0.34	0.30	0.40	0.48	0.52	0.45
Nb	0.98	1.02	1.05	1.00	0.92	1.39	1.16	0.84	0.69	1.14	1.02

### 3.3. Effects of Overheating Conditions

Overheating of PHS, be it due to escalating furnace temperature and/or extended residence time in the furnace, can result in unwanted coarsening of the PAGS. Niobium microalloying has been previously shown to obstruct PAGS coarsening during overheating. The anticoarsening performance of the current NbV PHS was checked for three conditions of increasing severity ( $H_p$  parameter), as reported in Table 6.

**Table 6.** Prior austenite grain size (PAGS) evolution for increasing heat treatment severity, defined by the Hollomon parameter ( $H_p = T/1000 \cdot (20 + \log(t))$ , temperature T in K, time t in s).

HT condition $H_p$ parameter	915 °C × 8'	915 °C × 25'	970 °C × 8'	970 °C × 25'
Standard PHS: PAGS range (µm)	15–20	30–40	30–55	130–150
NbV PHS: PAGS range (µm)	10–15	20–30	15–35	50–70

The composition analysis of individual nanoparticles revealed that Nb and Ti are again present in approximately equal amounts, whereas the share of V has decreased to around 10% after the most severe heat treatment (970 °C × 25 min). Figure 7 shows EDX mappings of a particle array, highlighting the depletion of vanadium. Accordingly, vanadium must have partially dissolved from particles that originally had a higher average content, as was shown before. Furthermore, it appears that the particles have grown in size by overaging, thereby reducing grain coarsening resistance.

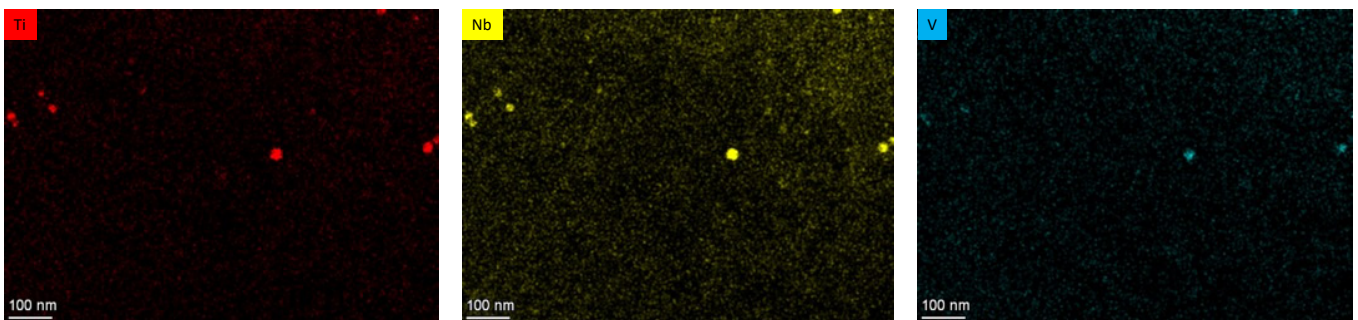


**Figure 7.** EDX mapping of the nanoparticles after severe overheating (970 °C × 25').

Overheating also affects the mechanical properties, as can be recognized from the representative tensile curves in Figure 8. At moderate overheating severity (915 °C × 25'), strength increases relative to the reference treatment, and despite the observed coarsening of the PAGS. The strength loss due to coarsening is estimated to be 40 MPa, while the measured strength increase is 40 MPa. Thus, effectively 80 MPa must be provided by additional precipitation strengthening. For the highest overheating severity, strength significantly decreases. The yield strength difference, as compared to the reference treatment, is around 120 MPa. Approximately 100 MPa can be related to the observed grain coarsening. The balance must originate from particle coarsening due to overaging.

### 3.4. Precipitation during Paint Baking Treatment

The paint baking procedure, typically performed at 170 °C for the duration of 20 min, represents a low-temperature tempering treatment of the as-quenched martensite. This will not affect microalloy carbides, but can lead to the formation of additional ferrous carbides. Samples of quenched standard PHS (22MnB5) were bake-treated and subsequently characterized by TEM analysis. A homogeneous population of rod-like particles is observed within martensite laths (Figure 9a). These particles grow along preferred crystallographic orientations with respect to the host matrix [21]. Their dimensions are about 100 nm in length and about 10 nm in thickness, as can be recognized from the particle size distribution analysis (Figure 9b).

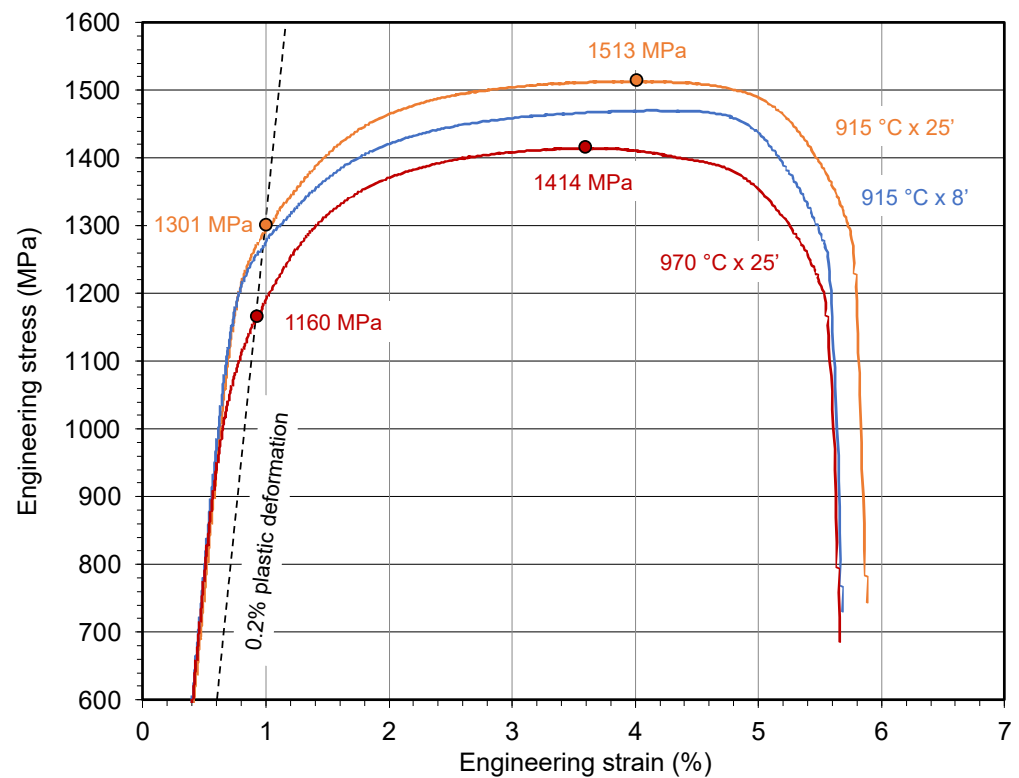


**Figure 8.** Tensile curves of NbV PHS for different heat treatment severities, followed by simulated die quenching (strength data for reference treatment see Table 4).

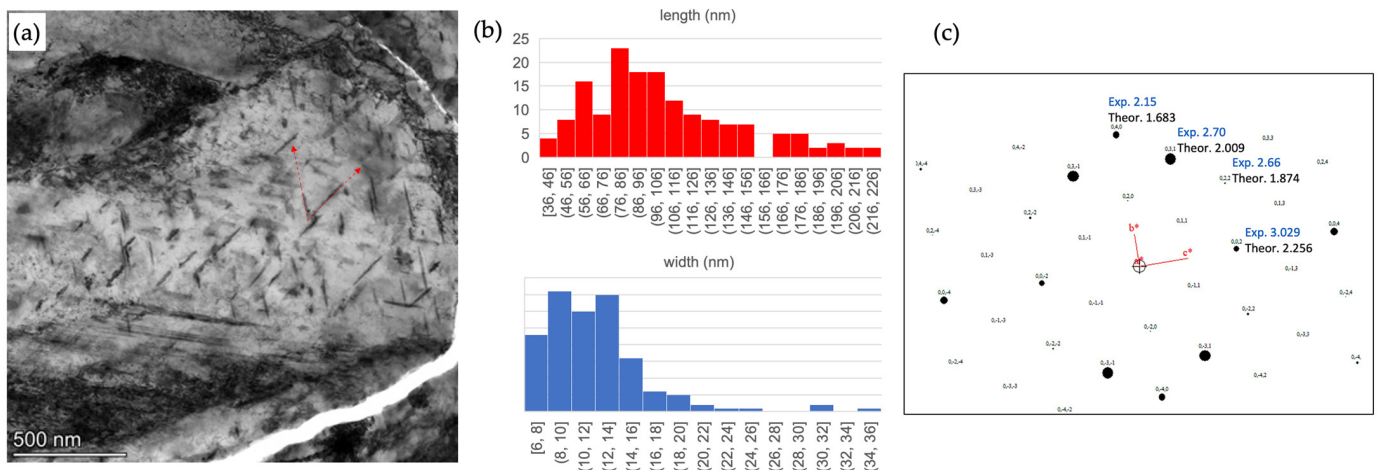


**Figure 9.** (a) TEM micrograph showing a population of oriented rod-shaped transitional iron carbides in the standard PHS (22MnB5). (b) Length and width distribution of iron carbide rods. (c) Selected area electron diffraction pattern indexed according to an orthorhombic structure isomorphous to cementite ( $\text{Fe}_3\text{C}$ ), zone axis  $[1\ 0\ 0]$ .

The EDXS spectra of these particles reveal that their composition is carbon rich. It is concluded that these particles are iron carbides, with a crystal structure between those of  $\epsilon$ -carbide and cementite. The analysis of selected area electron diffraction (SAED) patterns revealed that the rod-shaped precipitates had an orthorhombic crystallographic structure, isomorphous to cementite ( $\text{Fe}_3\text{C}$ ), but presented lattice parameters 30% larger than those of cementite. The interface between these transitional ferrous carbides and the matrix is hence assumed to be incoherent.

In the NbV PHS, such ferrous carbides are sparsely scattered and are found only in a few areas, as shown in Figure 10a. These areas are typically located near boundaries. In

other cases, ferrous carbides appear to have nucleated close to microalloy nanoparticles (Figure 10b,c).

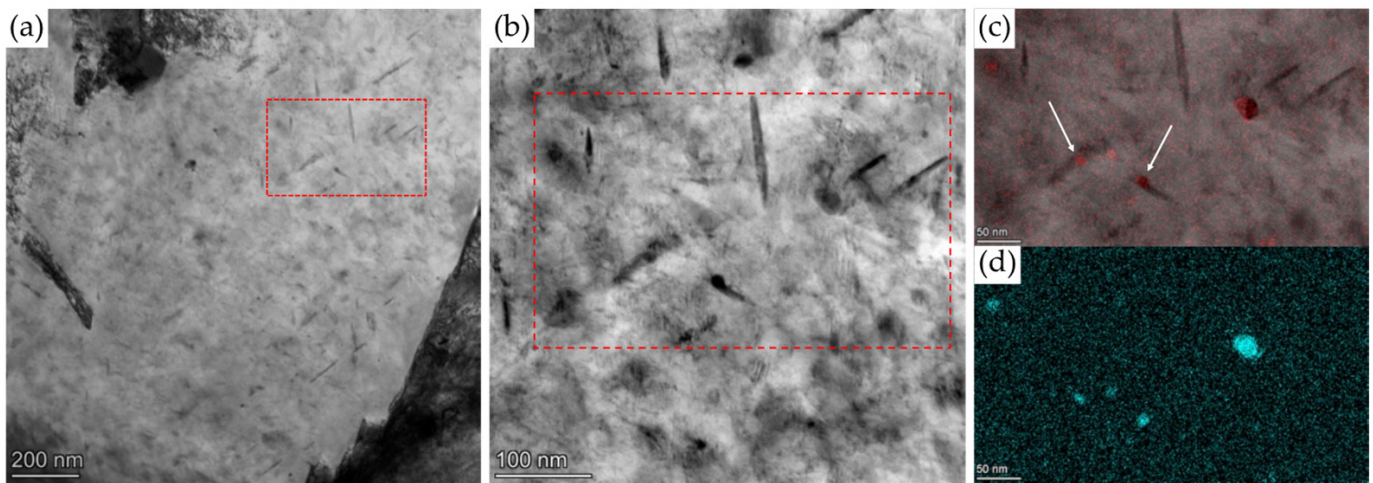


**Figure 10.** (a) TEM micrograph showing sparsely scattered transitional iron carbides in the NbV PHS. (b) Iron carbide formation in an area of microalloy nanoparticles identified as being rich in Ti (c) and V (d), as well as containing a minor share of Nb.

#### 4. Discussion

The observation that the standard 22MnB5 steel significantly coarsens under increasingly severe heating conditions indicates a lack of the Zener pinning force. A high density of ultrafine particles with homogeneous spatial distribution, as present in the NbV-modified PHS, successfully counteracts grain coarsening. This effect is known from many other studies on heat-treatable steels.

The microscopic analysis revealed the presence of very coarse primary TiN particles (Figure 2a), and a population of titanium carbonitride particles in the size range of 50–200 nm, in the final heat-treated condition of the standard PHS (22MnB5). Some of these particles were associated with CuS precipitates. However, ultrafine carbide precipitates with sizes in the lower nanometer range were not observed after heat treatment, despite a rather high excess amount of titanium over the stoichiometric Ti:N ratio. Since press hardening steel is usually not subjected to austenite conditioning (controlled rolling), substantial strain-induced precipitation of Ti in austenite cannot be expected. Figure 11 represents a simple estimation of the solubility of binary microalloy carbides, assuming a carbon content of 0.2% [22–24]. While the solubility of titanium at a lower austenite temperature is very low, precipitation kinetics are too slow for reaching equilibrium [12]. However, the residual solute titanium content precipitates during or after phase transformation to ferrite, typically in form of nanosized particles. The fact that such particles could not be found suggests that ultrafine TiC particles must have disappeared during subsequent heat treatment.

It must be considered, however, that only in full austenite does the dissolved carbon correspond to the actually alloyed amount, while the maximum soluble carbon content in ferrite is limited by the line G-P'-Q in the iron–carbon phase diagram [25]. Accordingly, the maximum solute carbon amount is around 0.022% at  $A_1$  temperature, and continuously decreases towards  $A_3$  temperature. The solute carbon concentration in the coexisting austenite fraction equivalently increases by partitioning. While this effect is quantitatively rather marginal in the austenite phase, it can be quite significant in the ferrite phase, as was experimentally demonstrated by Nöhner et al. [26]. To substantiate this difference, Figure 11 shows the microalloy solubility for a very low carbon content of 0.01%. Accordingly, TiC and NbC are practically insoluble at lower austenite temperatures, as well as in ferromagnetic ferrite, i.e., below the Curie temperature of around 770 °C. However, in the intercritical temperature range, the solubility of Ti and V reaches relevant proportions that could result in either partial or complete particle dissolution. The time for dissolving

nanosized microalloy particles is extremely short [27]. Thus, partial dissolution can already occur during upheating cycles, and does not require extended holding periods. Vanadium carbide solubility is also significant in austenite within the intercritical temperature range, while this is not the case for niobium and titanium.

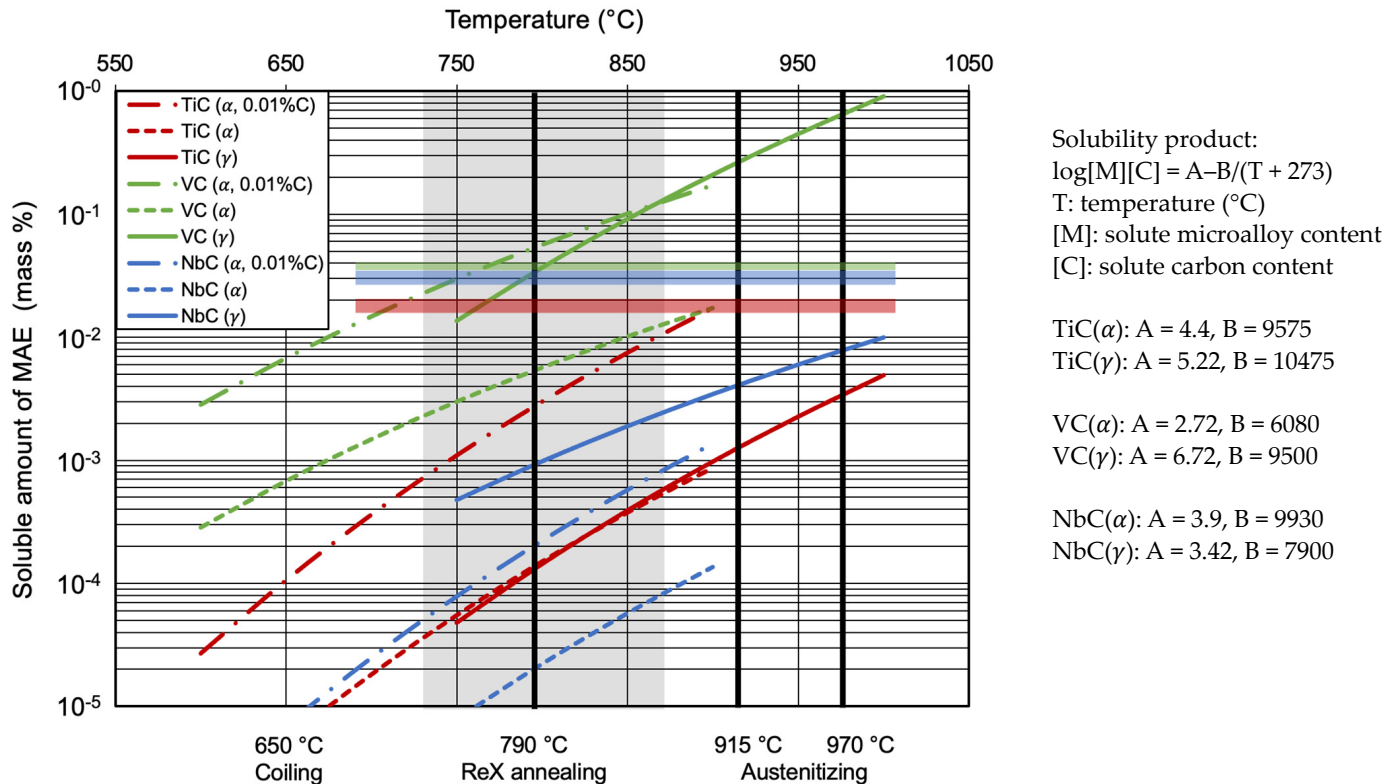


**Figure 11.** Microalloy carbide solubility (acc. to listed solubility products [22–24]) in ferrite ( $\alpha$ ) and austenite ( $\gamma$ ) for a nominal carbon content of 0.2% at indicated treatment conditions (dashed-dotted line represents solubility in ferrite containing 0.01% C); microalloying element is fully solute if the solubility curve is above the respective horizontal bar; grey shaded area represents the intercritical temperature range.

Yet, it is uncertain whether such a simplified dissolution scenario of microalloy carbides in the intercritical temperature range represents reality. Data from earlier experimental studies, however, seem to support the hypothesis of partial dissolution. In a previous study, dual-phase steels of identical base composition (0.1% C), microalloyed with either niobium (0.03%) or vanadium (0.12%), were intercritically annealed at 800 °C and subsequently quenched [28]. The precipitate status in the quenched steels was evaluated by a chemical extraction technique. The results indicated that niobium remained fully precipitated, but about 70% of the original vanadium content was dissolved. A detailed analysis on the precipitation behavior of niobium in a 0.2% C dual-phase steel indicated that intercritical annealing at 850 °C preserves niobium precipitates, most of them having ultrafine size [29]. A study on Ti and V microalloyed TRIP steels containing around 0.3% C revealed that the volume fraction of TiC and VC decreased with increasing intercritical annealing temperature [30]. Thus, both species dissolved in high-temperature ferrite. Based on such experimental evidence, a dedicated theoretical approach should be worked out, allowing reliable estimation of microalloy solubility in intercritical ferrite.

Exposing a population of microalloy carbide particles to high temperatures during intercritical annealing or soaking in austenite can cause various metallurgical effects:

1. Particle (partial) dissolution.
2. Particle coarsening (Ostwald ripening).
3. Loss of particle coherency.

4. Particles spheroidization in the fcc matrix.
5. Compositional changes in mixed microalloy carbides.

Under the condition of partial dissolution, the dissolved species can provide solute feedstock, enabling coarsening of neighboring particles. This requires that the diffusion range of dissolved atoms is comparable to the average interparticle distance. The diffusion range of microalloying elements for diffusion constants applicable to the paramagnetic ferrite state existing above the Curie temperature [31–33] is represented in Figure 12a. At lower ferrite temperatures, the diffusivity of microalloying elements is significantly reduced due to lattice stiffening by magnetic spin ordering [34]. It is evident that for the condition of recrystallization annealing, the diffusion range is sufficient in comparison to typical interparticle spacing (grey shaded area). Figure 12b shows the diffusion range of microalloy atoms in austenite according to the processing parameters used in this study. Again, the requirement for particle coarsening is fulfilled. Another important parameter influencing the tendency for particle coarsening is the interfacial energy per unit area between the particle and the bcc matrix. This interfacial energy has been determined by ab initio calculations [35,36], to the order  $TiC > VC > NbC$ . Accordingly, TiC has the relatively strongest tendency for particle coarsening.

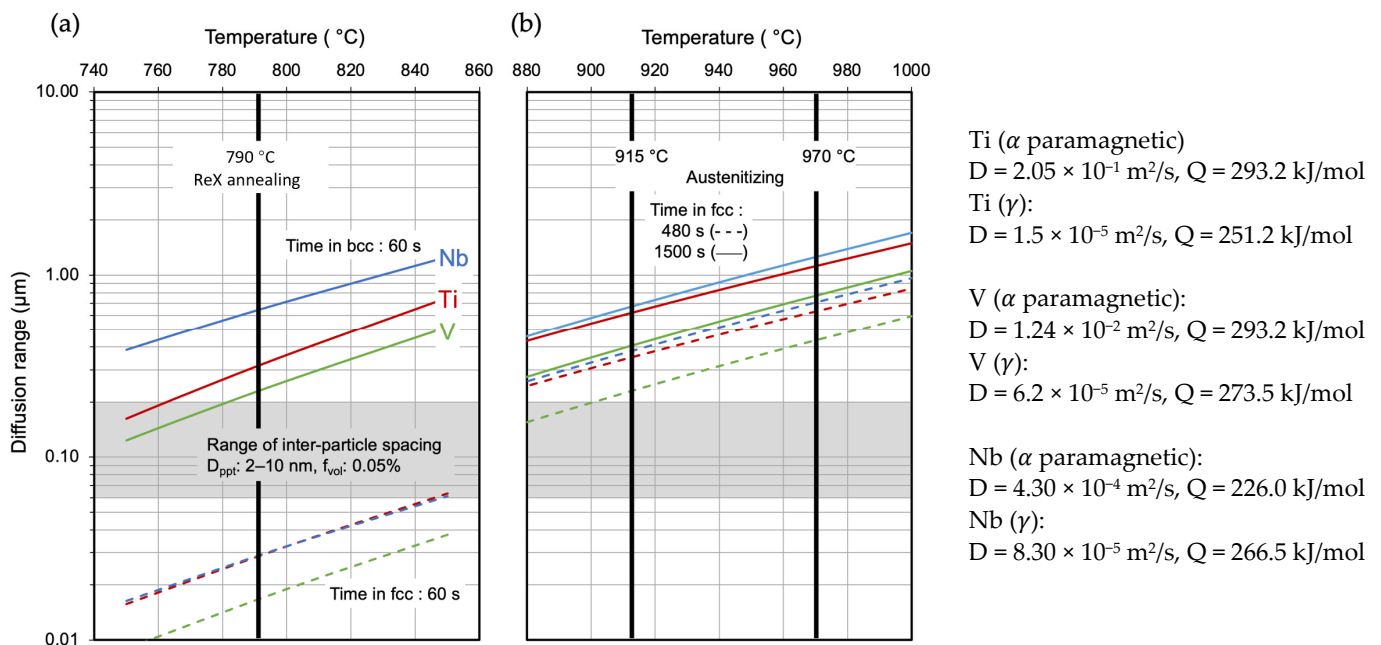


**Figure 12.** Calculated diffusion range (diffusion data [31–33]) of microalloying elements in paramagnetic ferrite (a) and austenite (b) as a function of temperature for holding times, as indicated (left: recrystallization (ReX) annealing after cold rolling, right: austenitizing before hot stamping). The grey shaded area represents the typical range of interparticle spacing between precipitates for comparison.

A mixing entropy contribution enhances the stability of Nb–Ti–V carbide particles over that of binary carbides, as described by Zou and Kirkaldy [37]. A recent work demonstrated the increased stability of mixed Nb–Ti carbides even at high austenite temperatures, which can be of great relevance to grain size control during welding [38].

According to Hin et al. [39], heterogeneous dislocation precipitation of microalloy carbide nucleation starts from transient FeC precipitates formed after fast segregation of carbon at dislocations. Slower diffusing microalloy atoms progressively replace iron atoms in these transient FeC precipitates. Another possible mechanism is carbide formation from isostructural diffuse atmospheres of microalloy atoms and carbon [40]. Microalloy carbides (TiC, NbC, and VC) precipitating into ferrite typically accept a Baker–Nutting orientation relationship with the host lattice. Accordingly, the particle attains a disc-like shape. The

precipitation kinetics is controlled by the driving force (formation energy) and the strain energy related to the lattice misfit at the coherent interface. The driving force is largest for TiC, while the misfit strain energy is highest for NbC. Therefore, precipitation kinetics is expected to be fastest for TiC, and slowest for NbC. VC can facilitate particle nucleation since its misfit strain energy is particularly low. Therefore, a scenario of forming mixed Ti–Nb–V carbides is most probable and corresponds to the experimental observations in this study.

When heating up to the austenitizing temperature, and upon full transformation to austenite, aging of the existing precipitate population occurs. From the tensile behavior shown in Figure 8, it is perceived that peak-aging occurred after around 25 min holding at 915 °C. The estimated diffusion ranges, shown in Figure 12, are sufficient to enable particle coarsening. All disc-shaped particles that precipitated in ferrite with a coherent interface should spheroidize and become incoherent [29]. Under plastic deformation, moving dislocations pass incoherent particles by Orowan looping [41]. This mechanism generates additional work hardening, resulting not only in higher tensile strength, but simultaneously in better elongation. Particle overaging under a most severe overheating condition has the opposite effect, which is also reflected in the respective tensile curve (Figure 8). During the austenitizing period, the solubility of vanadium is higher than its available content (Figure 11). Vanadium atoms, concentrated in the outer layers of mixed carbide particles, can progressively redissolve with increasingly severe overheating conditions, as was observed in Figure 7. The large diffusion range (Figure 12) allows homogenization of the redissolved vanadium in the matrix. Reprecipitation during quenching is not possible for kinetic reasons, whereas precipitation could occur during high-temperature tempering or in the heat-affected zone of welds.

The formation of transitional ferrous carbides during low-temperature tempering requires efficient diffusion of interstitial carbon. However, carbon tends to segregate at high-angle and low-angle boundaries, as well as at dislocations upon martensite transformation. Speich [42] demonstrated that all interstitial carbon can be trapped in martensitic C–Mn steels with carbon contents up to 0.2 mass percent. The investigated NbV PHS, with 0.2% C, of which a small part (estimated to be 130 ppm) is fixed in microalloy precipitates, meets this condition. Furthermore, due to the smaller PAGS, increased storage capacity by high-angle boundaries is provided. It has been demonstrated by atom probe tomography that carbon forms a segregation profile across the prior austenite grain boundary, with a several atom percent peak concentration and a profile width of around 10 nanometers [43,44]. Thus, it is indeed feasible that generally insufficient diffusible carbon is available for forming ferrous carbides in the NbV PHS. The few ferrous carbides observed may be originating from a locally available diffusible carbon. The preferred orientation of these ferrous carbide rods, as well as their interspacing, suggests that they form along martensite lath boundaries (Figure 10a). At these low-angle boundaries, carbon trapping might be relatively weak, while simultaneously the lath boundary represents a suitable nucleation site. It is also possible that the considerable excess of solute vanadium in the matrix plays a role by its attractive interaction with interstitial carbon atoms, thus, reducing their mobility. Figure 10b–d identifies rod-like iron carbides in the vicinity of particularly vanadium-rich precipitates, with an average Ti:Nb:V ratio of 1:0.25:1.38. Accordingly, the solute vanadium concentration, and thus V–C atomic interactions, should be reduced in the adjacent matrix. These possible explanations, however, need to be substantiated by a more detailed investigation.

Based on the present results and insights, as well as previous research on multiple microalloyed PHS, it is possible to formulate recommendations regarding alloy concepts that provide grain coarsening resistance and a particle-based hydrogen trapping capacity. It became clear that titanium-only, i.e., standard, PHS does not provide the desired functionality. Accordingly, excess addition of titanium well above the stoichiometric Ti:N ratio is not conducive. On the contrary, excess titanium promotes primary precipitation of TiN particles, which are detrimental to properties related to fracture toughness. A solubility

consideration (Figure 13a) indicates that this even holds for the very low nitrogen content (30 ppm) in the present steels. Accordingly, the nominal concentration ratio predicts that TiN should precipitate below approximately 1400 °C, i.e., in fully solidified austenite. However, during solidification, titanium and nitrogen segregate at interdendritic liquid pools, accumulating a much higher concentration (Figure 13b). The segregation ratios of the elements titanium and nitrogen are plotted as a function of the remaining liquid volume fraction in Figure 13b using Scheil's equation [45] and distribution coefficients compiled by Morita and Tanaka [46]. The local oversaturation triggers primary TiN precipitation, leading to large particle sizes often arranged in ribbon-like clusters [12]. The impact of the Ti:N ratio on the TiN particle size distribution in PHS was experimentally confirmed by Milani et al. [47]. Reducing the titanium content closer to the stoichiometric Ti:N ratio could largely suppress the occurrence of primary TiN particles, especially in the current low-nitrogen steels. Even slightly substoichiometric titanium addition can protect a sufficiently high amount of boron for providing full hardenability. In steels produced via the electric arc furnace melting, with typical nitrogen contents of 90–120 ppm, it is nearly impossible to avoid coarse TiN particles without prior vacuum degassing of the liquid steel.

Dual microalloying of titanium and vanadium can provide a stable nanoparticle population along the press hardening processing route. The experimental results by Cho et al. [8], in agreement with the current interpretation, indicated that TiC and VC were present after coiling and, particularly the particle fraction of VC, augmented during recrystallization annealing. Thus, VC precipitating as a layer around pre-existing TiC particles can prevent the dissolution of TiC at that stage. However, after austenitizing at 900 °C for 5 min (i.e., at lower annealing severity than any of the current treatments), a large part of the VC particles had redissolved while the TiC particles, insoluble in austenite, survived. In fact, only 0.05% out of the actual 0.2% vanadium added to these 30MnB5 and 35MnB5 steels was finally represented in VC particles. The systematic comparison of multiple microalloying concepts in 22MnB5 by Liu et al. [18] indicated that single microalloying with titanium does not provide coarsening resistance. Dual TiV microalloying results in moderate coarsening resistance, whereas NbTi microalloying shows strong coarsening resistance. Triple microalloying (NbTiV), however, brings only a marginal advantage over dual NbTi microalloying.

Therefore, the dual NbTi alloy concept, with restricting titanium close to the stoichiometric Ti:N ratio, appears to be the most suitable choice for achieving enhanced PHS performance. Thereby, the optimum niobium microalloy addition is around 0.05%. On the one hand, this amount of niobium approaches the maximum content that can be brought into solution at common slab reheating temperatures of 1230–1250 °C. On the other hand, opting for lower niobium addition might provide insufficient functionality, since part of the added niobium (100–200 ppm) will be scavenged by coarser TiN particles. The number density of MC particles cannot be arbitrarily increased by simply adding a higher microalloying content, since particle nucleation is controlled by the distribution of incipient nucleation sites. Experience with precipitation-strengthened ferritic–pearlitic HSLA steels indicates that the strength increase levels off in the range of 0.05–0.08% Nb addition. Previous research on niobium microalloyed PHS has indicated that an addition of 0.05% appears to be the optimum in terms of resistance against grain coarsening, as well as hydrogen cracking [3,9,44,48,49]. Thereby, the entire precipitate size distribution must be considered, rather than using average values. Respective modelling of grain coarsening resistance during annealing in austenite showed good agreement with the experimental data in NbTi microalloyed steels [50].

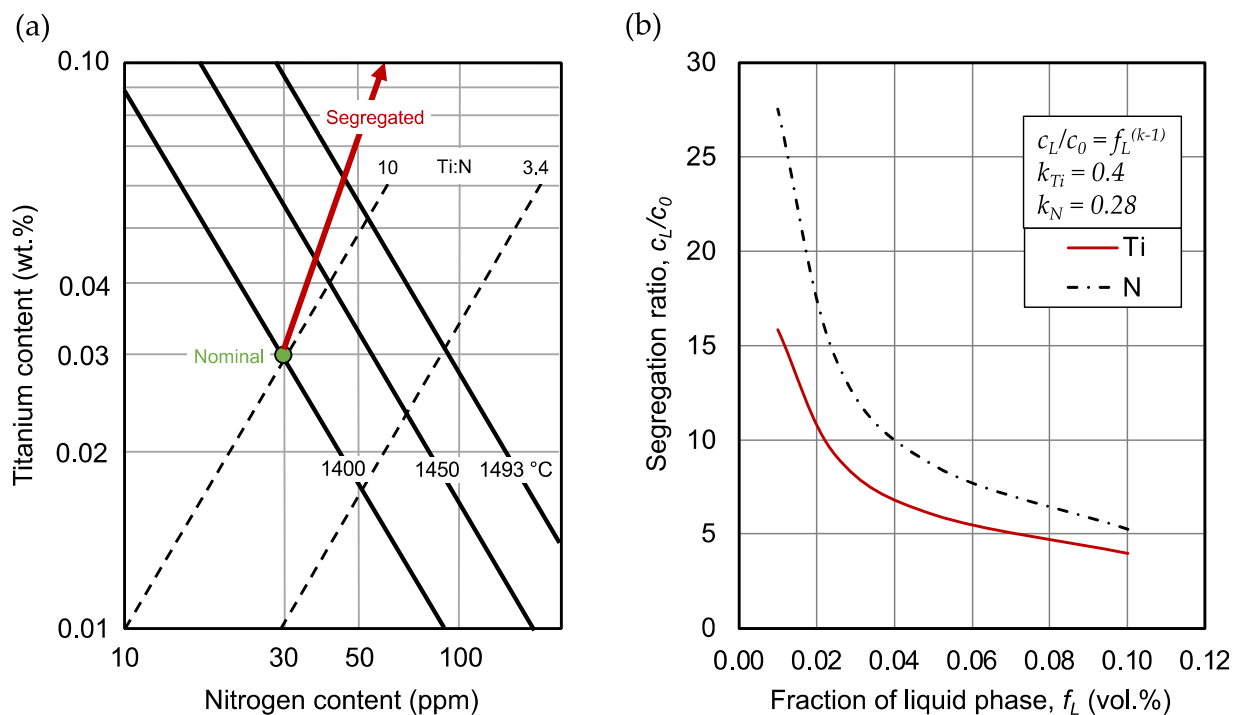


**Figure 13.** (a) Solubility limits of titanium and nitrogen in high-temperature austenite ( $1493\text{ }^{\circ}\text{C}$  = peritectic temperature), indicating the risk of primary TiN precipitation ( $\log[\text{Ti}][\text{N}] = 5.4 - 15,790/(273 + T)$ ) [51]. (b) Segregation ratio of Ti and N in late solidifying liquid pools calculated according to Scheil's equation using the indicated distribution coefficients (see insert).

## 5. Conclusions

The results of this study, based on transmission electron microscopy, confirmed that single titanium microalloying does not provide a stable nanoprecipitate population obstructing grain coarsening during the austenitizing treatment before hot stamping. This was reasoned by partial dissolution and Ostwald ripening of titanium carbide particles in the intercritical temperature range. Titanium nitride particles are stable in ferrite and up to very high austenite temperatures but are too inhomogeneously distributed to fulfil the desired functionality.

Nb–Ti–V mixed carbide particles are stable over the entire ferrite, as well as the relevant austenite, temperature range. These particles have an ultrafine size and comprise a homogeneous spatial distribution. Therefore, Nb–Ti–V mixed carbide particles are well suited for grain size control, especially under overheating conditions.

The vanadium share in these mixed particles represents only around 20 percent of its total microalloyed amount under standard heat treatment conditions. Under more severe austenitizing conditions (overheating), the vanadium share in the particles is further reduced due to partial dissolution.

Hence, a dual microalloying concept, with the titanium content limited to around the stoichiometric ratio with nitrogen (Ti:N = 3.4:1), and a niobium content of approximately 0.05 mass percent, appears to be the optimum solution in terms of particle stability and alloy cost.

**Author Contributions:** Conceptualization, F.D., S.G. and R.V.; methodology, L.B., M.T. and G.I.; validation, L.B., H.M. and M.T.; formal analysis, H.M., L.B. and G.I.; writing—original draft preparation, H.M.; writing—review and editing, L.B., M.T., G.I., S.G. and R.V.; project administration, F.D. All authors have read and agreed to the published version of the manuscript.

**Funding:** This research received no external funding.

**Conflicts of Interest:** The authors declare no conflict of interest.

## References

1. Philippot, C.; Beauvais, M.; Sarkar, S.; Cobo, S.; Lucas, E.; Thillou, B.; Drillet, P. Advanced Cleanliness Control in the 2nd Generation of Press Hardened Steels Produced by ArcelorMittal. In *Advanced High Strength Steel and Press Hardening, Proceedings of the 4th International Conference on Advanced High Strength Steel and Press Hardening (ICHSU2018), Hefei, China, 20–22 August 2018*; World Scientific: Singapore, 2019; pp. 551–559.
2. Pang, J.C.; Yi, H.L.; Lu, Q.; Enloe, C.M.; Wang, J.F. Effect of TiN-Particles on Fracture of Press-Hardened Steel Sheets and Components. *JOM* **2019**, *71*, 1329–1337. [[CrossRef](#)]
3. Mohrbacher, H. Property Optimization in As-Quenched Martensitic Steel by Molybdenum and Niobium Alloying. *Metals* **2018**, *8*, 234. [[CrossRef](#)]
4. Zheng, X.; Ghassemi-Armaki, H.; Hartwig, K.T.; Srivastava, A. Correlating Prior Austenite Grain Microstructure, Microscale Deformation and Fracture of Ultra-High Strength Martensitic Steels. *Metals* **2021**, *11*, 1013. [[CrossRef](#)]
5. Enloe, C.M.; Mohrbacher, H. Influences of Martensite Morphology and Precipitation on Bendability in Press-Hardened Steels. *SAE Int. J. Adv. Curr. Pract. Mobil.* **2022**, *4*, 1181–1188. [[CrossRef](#)]
6. Cai, H.L.; Wang, J.F.; Wu, D.; Yi, H.L. A Simple Methodology to Determine Fracture Strain of Press-Hardened Steels Under Plane Strain Bending. *Metall. Mater. Trans. A* **2021**, *52*, 644–654. [[CrossRef](#)]
7. Gui, L.; Zhao, Y.; Feng, Y.; Ma, M.; Lu, H.; Tan, K.; Chiu, P.-H.; Guo, A.; Bian, J.; Yang, J.-R.; et al. Study on the Improving Effect of Nb-V Microalloying on the Hydrogen Induced Delayed Fracture Property of 22MnB5 Press Hardened Steel. *Mater. Des.* **2023**, *227*, 111763. [[CrossRef](#)]
8. Cho, L.; Seo, E.J.; Sulistiyo, D.H.; Jo, K.R.; Kim, S.W.; Oh, J.K.; Cho, Y.R.; de Cooman, B.C. Influence of Vanadium on the Hydrogen Embrittlement of Aluminized Ultra-High Strength Press Hardening Steel. *Mater. Sci. Eng. A* **2018**, *735*, 448–455. [[CrossRef](#)]
9. Mohrbacher, H. Martensitic Automotive Steel Sheet—Fundamentals and Metallurgical Optimization Strategies. *Adv. Mater. Res.* **2014**, *1063*, 130–142. [[CrossRef](#)]
10. Jian, B.; Wang, L.; Mohrbacher, H.; Lu, H.Z.; Wang, W.J. Development of Niobium Alloyed Press Hardening Steel with Improved Properties for Crash Performance. *Adv. Mater. Res.* **2014**, *1063*, 7–20. [[CrossRef](#)]
11. Rosenstock, D.; Gerber, T.; Castro Müller, C.; Stille, S.; Banik, J. Process Stability and Application of 1900 MPa Grade Press Hardening Steel with Reduced Hydrogen Susceptibility. *IOP Conf. Ser. Mater. Sci. Eng.* **2022**, *1238*, 012013. [[CrossRef](#)]
12. Webel, J.; Herges, A.; Britz, D.; Detemple, E.; Flaxa, V.; Mohrbacher, H.; Mücklich, F. Tracing Microalloy Precipitation in Nb-Ti HSLA Steel during Austenite Conditioning. *Metals* **2020**, *10*, 243. [[CrossRef](#)]
13. Wang, J.; Enloe, C.; Singh, J.; Horvath, C. Effect of Prior Austenite Grain Size on Impact Toughness of Press Hardened Steel. *SAE Int. J. Mater. Manuf.* **2016**, *9*, 488–493. [[CrossRef](#)]
14. Cobo, S.; Sturel, T.; Aouafi, A.; Allely, C.; Cornette, D. Hydrogen Embrittlement Resistance of Al-Si Coated 1.8GPa Press Hardened Steel Solutions for Body-in-White (BIW) Applications. In *Proceedings of the 7th International Conference on Hot Sheet Metal Forming of High Performance Steel, Luleå, Sweden, 2–5 June 2019*; pp. 179–189.
15. Maikranz-Valentin, M.; Genchev, G.; Mirkovic, D. Improvement of Hydrogen Embrittlement Resistance of Press-Hardening Steels. In *Proceedings of the 7th International Conference on Hot Sheet Metal Forming of High Performance Steel, Luleå, Sweden, 2–5 June 2019*; pp. 611–618.
16. Holzweissig, M.J.; Frost, G.; Bake, K.; Frehn, A. BTR2000—A New Uncoated Ultra-High Strength Hot Forming Steel. In *Proceedings of the 7th International Conference on Hot Sheet Metal Forming of High Performance Steel, Luleå, Sweden, 2–5 June 2019*; pp. 749–756.
17. Zhang, Z.; Wang, X.; Sun, Q.; Yang, B.; Xiong, L.; Liu, H. Study on Microstructure and Properties of Laser Dissimilar Welded Joints of Ultra-High Strength PHS1500/PHS2000 Steel. *Opt. Laser Technol.* **2022**, *150*, 107933. [[CrossRef](#)]
18. Liu, B.; Liao, X.; Tang, Y.; Si, Y.; Feng, Y.; Cao, P.; Dai, Q.; Li, K. Effects of the Addition of Nb and V on the Microstructural Evolution and Hydrogen Embrittlement Resistance of High Strength Martensitic Steels. *Scanning* **2022**, *2022*, 4040800. [[CrossRef](#)] [[PubMed](#)]
19. Vander Voort, G.F. *Metallography: Principles and Practice*; McGraw-Hill: New York, NY, USA, 1984.
20. de Almeida, D.T.; Clarke, T.G.R.; de Souza, J.H.C.; Haupt, W.; de Lima, M.S.F.; Mohrbacher, H. The Effect of Laser Welding on Microstructure and Mechanical Properties in Heavy-Gage Press Hardening Steel Alloys. *Mater. Sci. Eng. A* **2021**, *821*, 141341. [[CrossRef](#)]
21. Nagataki, Y.; Tsuyama, S.; Hosoya, Y.; Okita, T. Effect of Microstructure on Bendability of Ultra-High-Strength Steel Sheet. In *High-Strength Sheet Steels for the Automotive Industry*; Pradhan, R., Ed.; The Iron and Steel Society: Baltimore, MD, USA, 1994; pp. 239–244.
22. Taylor, K.A. Solubility Products for Titanium-, Vanadium-, and Niobium-Carbide in Ferrite. *Scr. Metall. Mater.* **1995**, *32*, 7–12. [[CrossRef](#)]
23. Narita, K. Physical Chemistry of the Groups IVa (Ti, Zr), Va (V, Nb, Ta) and the Rare Earth Elements in Steel. *Trans. Iron Steel Inst. Jpn.* **1975**, *15*, 145–152. [[CrossRef](#)]
24. Sekine, H.; Inoue, T.; Ogasawara, M. Solubility of V<sub>4</sub>C<sub>3</sub> in  $\alpha$ -Iron. *Trans. Iron Steel Inst. Jpn* **1968**, *8*, 101–102. [[CrossRef](#)]
25. Ohtani, H.; Hasebe, M.; Nishizawa, T. Calculation of Fe-C, Co-C and Ni-C Phase Diagrams. *Trans. Iron Steel Inst. Jpn* **1984**, *24*, 857–864. [[CrossRef](#)]

26. Nöhrer, M.; Mayer, W.; Primig, S.; Zamberger, S.; Kozeschnik, E.; Leitner, H. Influence of Deformation on the Precipitation Behavior of Nb(CN) in Austenite and Ferrite. *Metall. Mater. Trans. A* **2014**, *45*, 4210–4219. [[CrossRef](#)]
27. Mohrbacher, H. Alloy Design and Processing Strategies for Grain Coarsening-Resistant Carburizing Steels. In Proceedings of the International Conference on Advances in Metallurgy of Long and Forged Products Proceedings, Online, 12–14 July 2021; Association for Iron & Steel Technology: Warrendale, PA, USA, 2021.
28. Mohrbacher, H. Effects of Niobium in Galvanized Advanced High Strength Steels for Automotive Applications. In Proceedings of the 7th International Conference on Zinc and Zinc Alloy Coated Steel Sheet, Osaka, Japan, 18–22 November 2007; pp. 386–391.
29. Mohrbacher, H.; Yang, J.-R.; Chen, Y.-W.; Rehr, J.; Hebesberger, T. Metallurgical Effects of Niobium in Dual Phase Steel. *Metals* **2020**, *10*, 504. [[CrossRef](#)]
30. Peng, J.; Jiang, H.; Zhang, G.; Chen, L.; Zhu, N.; He, Y.; Lu, X.; Li, L. In-Situ Analysis of Retained Austenite Transformation in High-Performance Micro-Alloyed TRIP Steel. *J. Iron Steel Res. Int.* **2017**, *24*, 313–320. [[CrossRef](#)]
31. Geise, J.; Herzig, C. Impurity Diffusion of Vanadium and Self-Diffusion in Iron. *Int. J. Mater. Res.* **1987**, *78*, 291–294. [[CrossRef](#)]
32. Klugkist, P.; Herzig, C. Tracer Diffusion of Titanium in  $\alpha$ -Iron. *Phys. Status Solidi (A)* **1995**, *148*, 413–421. [[CrossRef](#)]
33. Herzig, C.; Geise, J.; Divinski, S.V. Niobium Bulk and Grain Boundary Diffusion in Alpha-Iron. *Int. J. Mater. Res.* **2022**, *93*, 1180–1187. [[CrossRef](#)]
34. Fähnle, M.; Seeger, A. On the Magnetic Contribution to the Free Enthalpy of Vacancy Formation in Ferromagnetic Crystals. *Phys. Status Solidi (A)* **1985**, *91*, 609–617. [[CrossRef](#)]
35. Chung, S.-H.; Ha, H.-P.; Jung, W.-S.; Byun, J.-Y. An Ab Initio Study of the Energetics for Interfaces between Group V Transition Metal Carbides and Bcc Iron. *ISIJ Int.* **2006**, *46*, 1523–1531. [[CrossRef](#)]
36. Jang, J.H.; Lee, C.-H.; Heo, Y.-U.; Suh, D.-W. Stability of (Ti, M)C (M = Nb, V, Mo and W) Carbide in Steels Using First-Principles Calculations. *Acta Mater.* **2012**, *60*, 208–217. [[CrossRef](#)]
37. Zou, H.; Kirkaldy, J.S. Carbonitride Precipitate Growth in Titanium/Niobium Microalloyed Steels. *Metall. Trans. A* **1991**, *22*, 1511–1524. [[CrossRef](#)]
38. Webel, J.; Mohrbacher, H.; Detemple, E.; Britz, D.; Mücklich, F. Quantitative Analysis of Mixed Niobium-Titanium Carbonitride Solubility in HSLA Steels Based on Atom Probe Tomography and Electrical Resistivity Measurements. *J. Mater. Res. Technol.* **2022**, *18*, 2048–2063. [[CrossRef](#)]
39. Hin, C.; Bréchet, Y.; Maugis, P.; Soisson, F. Kinetics of Heterogeneous Dislocation Precipitation of NbC in Alpha-Iron. *Acta Mater.* **2008**, *56*, 5535–5543. [[CrossRef](#)]
40. Danoix, F.; Bémont, E.; Maugis, P.; Blavette, D. Atom Probe Tomography I. Early Stages of Precipitation of NbC and NbN in Ferritic Steels. *Adv. Eng. Mater.* **2006**, *8*, 1202–1205. [[CrossRef](#)]
41. Martin, J.W. *Micromechanisms in Particle-Hardened Alloys*; Cahn, R.W., Thompson, M.W., Ward, I.M., Eds.; Cambridge University Press: Cambridge, UK, 1980.
42. Speich, G.R. Tempering of Low-Carbon Martensite. *Trans. AIME* **1969**, *245*, 2553–2564.
43. Li, Y.J.; Ponge, D.; Choi, P.; Raabe, D. Segregation of Boron at Prior Austenite Grain Boundaries in a Quenched Martensitic Steel Studied by Atom Probe Tomography. *Scr. Mater.* **2015**, *96*, 13–16. [[CrossRef](#)]
44. Mohrbacher, H.; Senuma, T. Alloy Optimization for Reducing Delayed Fracture Sensitivity of 2000 MPa Press Hardening Steel. *Metals* **2020**, *10*, 853. [[CrossRef](#)]
45. Scheil, E. Bemerkungen Zur Schichtkristallbildung. *Int. J. Mater. Res.* **1942**, *34*, 70–72. [[CrossRef](#)]
46. Morita, Z.; Tanaka, T. Thermodynamics of Solute Distributions between Solid and Liquid Phases in Iron-Base Ternary Alloys. *Trans. Iron Steel Inst. Jpn.* **1983**, *23*, 824–833. [[CrossRef](#)]
47. Milani, A.; Philippot, C.; Lucas, E.; Cobo, S.; Gourgues, A.F. Effect of TiN Inclusions on the Crash Ductility Behaviour of Press Hardened Steels of 2nd Generation. In Proceedings of the Hot Sheet Metal Forming of High Performance Steel, Barcelona, Spain, 30 May–2 June 2022; pp. 487–494.
48. Zhang, S.; Huang, Y.; Sun, B.; Liao, Q.; Lu, H.; Jian, B.; Mohrbacher, H.; Zhang, W.; Guo, A.; Zhang, Y. Effect of Nb on Hydrogen-Induced Delayed Fracture in High Strength Hot Stamping Steels. *Mater. Sci. Eng. A* **2015**, *626*, 136–143. [[CrossRef](#)]
49. Zhang, S.; Wan, J.; Zhao, Q.; Liu, J.; Huang, F.; Huang, Y.; Li, X. Dual Role of Nanosized NbC Precipitates in Hydrogen Embrittlement Susceptibility of Lath Martensitic Steel. *Corros. Sci.* **2020**, *164*, 108345. [[CrossRef](#)]
50. Graux, A.; Cazottes, S.; de Castro, D.; San Martín, D.; Capdevila, C.; Cabrera, J.M.; Molas, S.; Schreiber, S.; Mirković, D.; Danoix, F.; et al. Precipitation and Grain Growth Modelling in Ti-Nb Microalloyed Steels. *Materialia* **2019**, *5*, 100233. [[CrossRef](#)]
51. Turkdogan, E.T. Causes and Effects of Nitride and Carbonitride Precipitation During Continuous Casting. *ISS Trans.* **1990**, *11*, 39–48.

**Disclaimer/Publisher’s Note:** The statements, opinions and data contained in all publications are solely those of the individual author(s) and contributor(s) and not of MDPI and/or the editor(s). MDPI and/or the editor(s) disclaim responsibility for any injury to people or property resulting from any ideas, methods, instructions or products referred to in the content.